



## Particle-induced viscous fingering

Feng Xu<sup>1</sup>, Jungchul Kim<sup>2</sup>, Sungyon Lee\*

Department of Mechanical Engineering, Texas A&M University, College Station, Texas, USA



### ARTICLE INFO

#### Article history:

Received 2 March 2016

Revised 27 June 2016

Accepted 27 June 2016

Available online 28 June 2016

#### Keywords:

Viscous fingering

Particle-laden flow

Shear-induced migration

Suspension balance model

### ABSTRACT

The Saffman–Taylor fingering instability arises when a less viscous fluid displaces a more viscous one inside porous media, which has been extensively studied for decades. Conversely, the invasion of a more viscous fluid into a less viscous fluid is inherently stable to interfacial instabilities. However, Tang et al. [1] first observed that the addition of particles to a viscous invading fluid can destabilize the fluid–fluid interface, even in the absence of the unstable viscosity ratio. Building on the previous observations, we experimentally characterize the particle-induced fingering patterns in a radial source flow for varying particle volume fractions and gap sizes. The onset of fingering is observed to be highly dependent on the particle volume fraction and also, to a lesser extent, on the channel gap thickness. The key physical mechanism behind this instability is the particle accumulation on the interface that stems from the *shear-induced migration* of particles far upstream of the interface. We model the particle-laden flow as a continuum in the quasi-steady region away from the interface, based on the suspension balance approach, and successfully validate the effects of shear-induced migration on the particle accumulation and subsequent fingering.

© 2016 Elsevier B.V. All rights reserved.

### 1. Introduction

Viscous fingering, one of the seminal problems in fluid mechanics, occurs when a less viscous fluid displaces a more viscous one in porous media [2–4]. Since its discovery, it remains an active area of research [5–7] due to its relevance in geophysical flows and other various phenomena, such as ribbing instability [8], balcony growth [9], dendritic growth [10], and flame propagation [11]. More recently, researchers have expanded the study of viscous fingering by focusing on techniques to control or modify fingering. For instance, the control of the viscous fingering instability was demonstrated by strategically modifying the channel geometry [12] or by modulating the elasticity of the channel walls [5]. Alternatively, viscous fingering can also be modified by changing the fluid phases themselves. For instance, incorporating non-Newtonian fluids, such as shear-thinning [13,14] and Boger [15] fluids, has shown to change the resultant fingering behaviors compared to their Newtonian counterpart.

In this paper, we focus on the viscous fingering instability that is specifically *induced* by the inclusion of non-colloidal particles in the displacing liquid. Given the prevalence of suspension flows

in geophysical systems, such as avalanches, as well as in industry that ranges from nanotribology to hydraulic fracturing, the study of interfacial instabilities in the presence of particles represents an exciting and relatively unexplored area of research. Tang et al. [1] first observed an unexpected interfacial instability when a mixture of non-colloidal particles and viscous fluid displaces air in a Hele–Shaw cell. Then, they qualitatively correlated the particle volume fraction,  $\phi_0$ , to the instability growth rate. It is noteworthy that the same flow without particles is inherently stable. More recently, Ramachandran & Leighton [16] observed the analogous fingering instability upon squeezing a particle–oil mixture between two parallel plates.

The mechanism of particle-induced fingering is the direct result of particle accretion on the fluid–fluid interface [1]. As the suspension viscosity is directly related to the local volume fraction, the increase in particle concentration leads to the viscosity gradient susceptible to miscible viscous fingering. The particle enrichment on the free surface has been previously observed in the suspension flow in a tube. For instance, Karnis & Mason measured the rate of particle accumulation on the meniscus in a tube flow [17]. The mechanism of the particle accumulation was later elucidated by Chapman [18] who attributed it to particles' tendency to migrate towards the regions of low shear stress, or *shear-induced migration* [19,20], upstream of the interface. More recently, Ramachandran & Leighton [21] incorporated the effects of gravity on the particle accumulation near meniscus in a tube flow and used the suspension

\* Corresponding author.

E-mail address: [sungyon.lee@tamu.edu](mailto:sungyon.lee@tamu.edu) (S. Lee).

<sup>1</sup> Co-lead author with equal contributions.

<sup>2</sup> Co-lead author with equal contributions.

**Table 1**

Experimental conditions tested; for all experimental runs, the flow rate  $Q$  and particle size  $D$  are kept constant at 150 mL/min and 125–150  $\mu\text{m}$ , respectively. A  $\phi_0$  range that is denoted as '# - #' increases by an increment of 1%.

$h$ (mm)	$\phi_0$ ( $\times 100\%$ )
0.6	10–18, 20–30 (increment of 1)
0.7	12–30
1.0	12–15, 17–32
1.2	14, 15, 17, 20–28, 30–35
1.3	8, 11, 14, 17, 20–35
1.4	8, 11, 14, 15, 17, 20–35

balance model [22] to implement the effects of shear-induced migration.

The suspension balance method [22] constitutes one of widely used continuum approaches to model particle-laden flows in the low Reynolds number limit, along with diffusive flux phenomenology [19,20,23,24] and, more recently, frictional suspension rheology that addresses the transition of suspension to granular media [25–28]. The diffusive flux model accounts for the particle migration via semi-empirical relationships between the particle flux and effective suspension viscosity and has been used to successfully model various flow configurations [20,23,24,29,30]. On the other hand, the suspension balance approach describes the particle migration due to the gradient in viscously generated particle stresses [22,31,32]. Distinct from the diffusive flux model, this method captures the rise in anisotropic normal stresses in dense suspensions. Due to its effectiveness in describing viscoelastic characteristics of the mixture in a non-dilute limit, the suspension balance model will be employed in the current analysis.

In the present work, we experimentally quantify the aforementioned particle-induced viscous fingering by injecting suspensions of varying  $\phi_0$  into a Hele–Shaw cell of varying gap thicknesses. We observe the particle accretion and identify the critical particle volume fraction at which the viscous fingering initiates. Image processing techniques are employed to measure the particle concentration as well as the extent of interfacial deformations. In parallel to experiments, we theoretically confirm the effects of shear-induced migration far upstream of the interface, based on the suspension balance method, in good agreement with the experimental data. The paper is organized as follows: in Section 2.1, we introduce our experimental setup and materials used in the experiments. The experimental analysis and results are summarized in Section 2.2, followed by our theoretical model in Section 3. The paper concludes with the summary and future directions in Section 4.

## 2. Experiments

### 2.1. Setup and materials

The Hele–Shaw cell consists of two plexi-glass (acrylic) plates (30.5  $\times$  30.5  $\times$  3.8 cm) that are leveled and separated to a gap thickness,  $h$ . The gap separation is controlled by securing shims (McMaster) of different sizes (listed in Table 1) in the four corners of the plates. The mixture is prepared by mixing a PMMS silicone oil (density  $\rho_1 = 0.96 \text{ g/cm}^3$  & viscosity  $\eta_1 = 0.096 \text{ Pa} \cdot \text{s}$ , UCT) and neutrally-buoyant polyethylene particles (density  $\rho_p = 1.00 \text{ g/cm}^3$ , Cospheric) with diameter,  $D = 125 - 150 \mu\text{m}$ , to an initial volume fraction,  $\phi_0$ . A syringe pump (New Era Pump Inc., Model NE-1010) is used to inject the mixture into the Hele–Shaw cell at a constant flow rate,  $Q = 150 \text{ mL/min}$ . An LED panel (EnviroOasis, 75W, 4200 Lumen) is placed under the Hele–Shaw cell to provide uniform illumination, while a Canon 60D camera (1920  $\times$  1080 pixel images,

FOV 64°) records the particle-laden flow from above at 30 frames per second with the spatial resolution of  $0.100 \pm 0.0075 \text{ mm}^2/\text{pixel}$  (schematic in Fig. 1(a)). All the experimental parameters tested are summarized in Table 1.

Images collected from the experiments are processed using MATLAB image processing toolbox. Once the images are cropped and smoothed with a median filter, the distance from the injection center to the suspension interface,  $R_b$ , (schematic in Fig. 1(b)) is extracted in each image using a built-in edge detection function. The edge detection code utilizes the ‘‘Canny’’ method that computes the local gradient of the image intensity field and identifies the maxima as edges. Unwanted noisy ‘‘edges’’ that do not meet the threshold number of data points are subsequently removed. In addition to computing the evolving shape of the interface, the variation in light intensity is also used to extract the local particle concentration inside the suspension, which will be elaborated in Section 2.2.

### 2.2. Experimental results

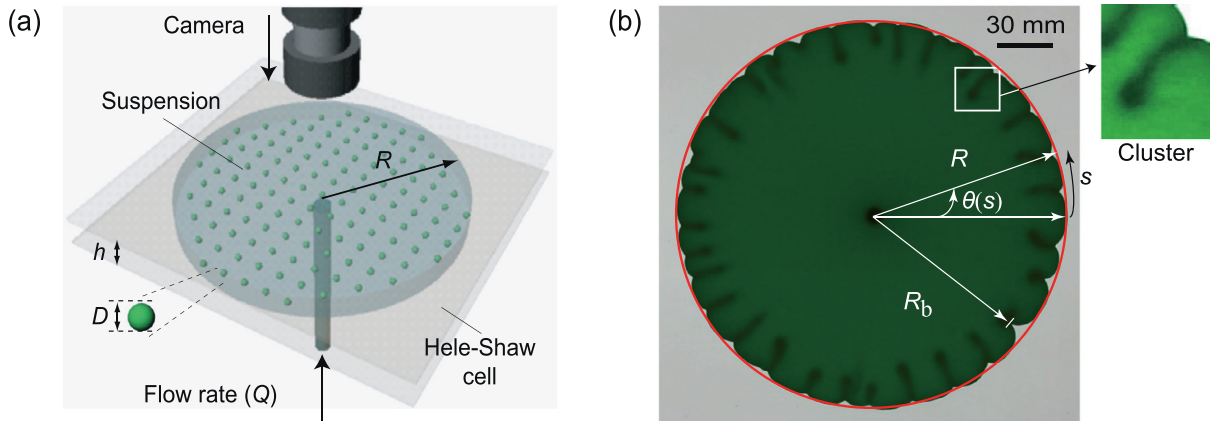
We inject the particle-oil mixture from the center of the Hele–Shaw cell by varying two key parameters: initial particle volume fraction,  $\phi_0$ , and the ratio of gap thickness to particle diameter,  $h/D$ . Fig. 1(b) shows a typical image of fingering at  $\phi_0 = 0.35$  and  $h/D = 10.2$ : as particles accumulate on the interface, the fluid–fluid interface deforms with growing particle clusters (see zoomed-in image of Fig. 1(b)). However, fingering does not occur in all conditions, as demonstrated in Fig. 2. At very low volume fractions, the distribution of suspension in the cell is uniform, with no resultant fingering. As  $\phi_0$  is increased, the particle accumulation on the meniscus becomes visible; finally, beyond some critical value of  $\phi_0$ , the interfacial deformations appear, accompanied by the formation of particle clusters.

Fig. 3(a) illustrates the time-elapsd comparison between typical low concentration ( $\phi_0 = 0.14$ ) and high concentration ( $\phi_0 = 0.35$ ) cases, while all the other parameters (*i.e.*  $h/D$ ,  $Q$ ) remain unchanged. At  $\phi_0 = 0.14$ , the interface remains circular over time, with the uniform distribution of particles throughout. At  $\phi_0 = 0.35$ , the interfacial deformations and particle cluster formation are first observed around time = 5.8 s. As the interface advances further, the fingering patterns do not significantly change in magnitude, while the particle clusters grow radially. Notably, the spatial distribution of interfacial fingers and particle clusters appears remarkably uniform for all times. In addition, the plot of the instantaneous radius,  $R_b$ , as a function of  $\theta$  in Fig. 3(b) clearly demonstrates the difference between the low and high concentration regimes;  $R_b$  at  $\phi_0 = 0.35$  strongly varies with  $\theta$  while that of  $\phi_0 = 0.14$  remains relatively uniform, which matches the qualitative observations.

The overall magnitude of interfacial deformation can be computed as a single dimensionless parameter,  $\Lambda$  [16], such that

$$\Lambda = \frac{1}{S} \int_0^S \left( 1 - \frac{R_b(s)}{R} \right)^2 ds, \quad (1)$$

where  $s$  refers to the curvilinear coordinate defined along the interface, while  $R$  is the radius of the best fitted circle of the area occupied by the suspension (notations given in Fig. 1(b)). As  $\Lambda$  characterizes the deviation of the instantaneous interface from a circle, it reduces to zero when  $R_b(s) = R$ , or the interface forms a perfect circle. Fig. 3(c) shows the plot of  $\Lambda$  versus  $R(t)/R_0$  for varying values of  $\phi_0$ . Consistent with our observations,  $\Lambda$  at early times appears to be independent of  $\phi_0$  for all cases within the margin of error [33]. The effect of  $\phi_0$  on  $\Lambda$  is evident at later times, as  $\Lambda$  rises much more significantly for larger  $\phi_0$ . However, overall the value of  $\Lambda$  remains in the order of  $10^{-4}$  even for large  $\phi_0$ , suggesting that the interfacial deformations are minimal, compared to



**Fig. 1.** (a) Schematic of the experimental setup: suspensions are injected into the Hele-Shaw cell from the center hole, and experimental observations are recorded with the camera from above. (b) Image of fingering phenomenon at  $\phi_0 = 0.35$ ,  $h/D = 10.2$ : both the interfacial deformations and particle clusters are clearly visible. The symbol,  $s$ , corresponds to the curvilinear coordinate defined along the edge;  $R_b$  is the instantaneous radius from the center to the interface, while  $R$  denotes the radius of the best fitted circle. The inset shows the zoomed image of the particle cluster that grows perpendicular to the interface.

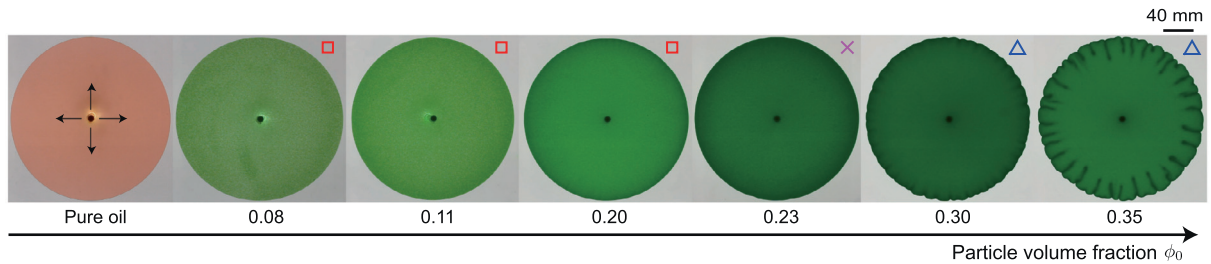


**Fig. 2.** Dependence of fingering phenomenon on initial particle volume fraction,  $\phi_0$ , is clearly demonstrated via the experimental images with  $h/D = 10.2$  and increasing  $\phi_0$ . At small  $\phi_0$ , the distribution of suspension remains quite uniform. Interfacial deformations are first observed at  $\phi_0 = 0.24$  and become more pronounced as  $\phi_0$  further increases. The black arrows in the pure oil case indicate the direction of the flow.

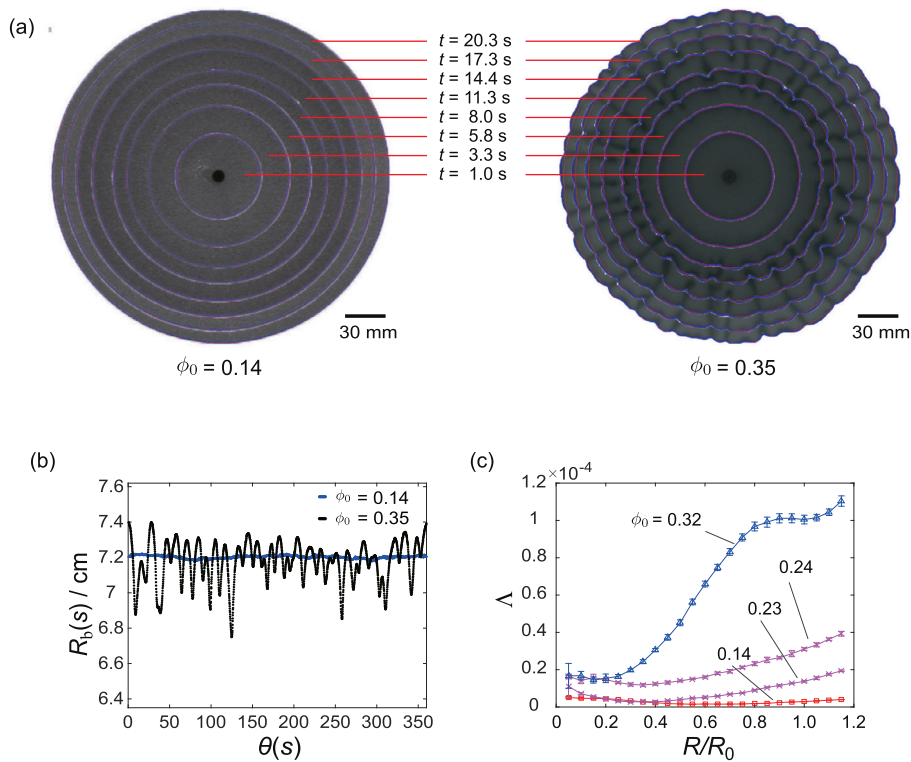


**Fig. 3.** (a) Time-elased images from two separate experimental runs:  $\phi_0 = 0.14$  (left) and  $\phi_0 = 0.35$  (right). At  $\phi_0 = 0.14$ , the shape stays almost circular over time, and the particle concentration appears uniform over the whole suspension. At  $\phi_0 = 0.35$ , interfacial deformations and particle clusters initially appear around  $t = 5.8$  s and are observed for all times thereafter. (b) The plot of the center-to-interface distance,  $R_b$  for  $\phi_0 = 0.14$  and  $0.35$  at  $h/D = 10.2$ . Consistent with the interfacial shapes in (a),  $R_b$  is nearly uniform for  $\phi_0 = 0.14$ , indicating a circular shape, while  $R_b$  for  $\phi_0 = 0.35$  strongly varies with  $\theta$ . (c) The plot of  $\Lambda$  over dimensionless time,  $R/R_0$ .

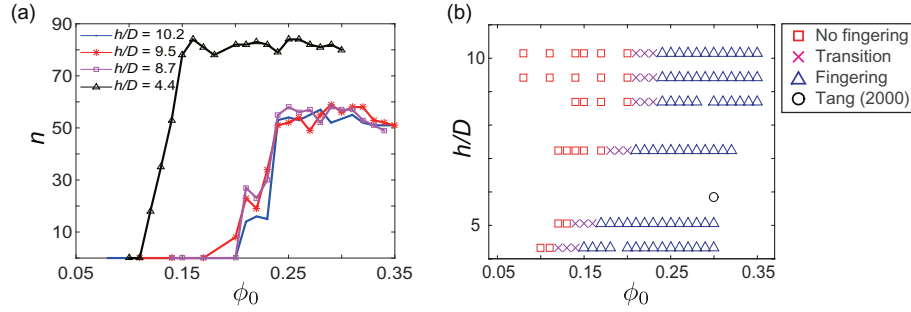


**Fig. 4.** (a) The number of total fingers,  $n$ , at  $R \approx 10$  cm is counted for all  $\phi_0$ . At  $h/D = 10.2$ , for instance, there is a sharp increase in  $n$  at  $\phi_0 = 0.23 - 0.24$  and plateaus to approximately 50 for large  $\phi_0$ . This transition point in  $n$  is used to systematically determine the boundary between “no fingering” and “fingering” regimes. (b) All experimental runs are organized into a phase diagram that shows the dependence of fingering instability on  $\phi_0$  and  $h/D$ . At large  $h/D$ , the boundary between no fingering (square) and fingering (triangle) appears to be independent of  $h/D$ ; however, the onset of fingering notably shifts to a smaller value of  $\phi_0$  as  $h/D$  decreases (the bottom three rows of data).

the classical viscous fingering with fractal-like patterns [7]. Interestingly, our fingering patterns are reminiscent of “stubby” fingers observed by Pilher–Puzovic and co-authors [5] who displaced oil with air in an elastic walled channel. In [5], the elastic membrane is shown to *stabilize* the unstable air-oil interface, hence, suppressing the growth of fingers. Similarly, in our present work, the inherently stable viscosity ratio between the suspension and air also suppresses interfacial deformations and yields “stubby” fingers.

Based on aforementioned observations and measurements, each experimental run can be organized into ‘no fingering’ versus ‘fingering’ regimes, for given  $\phi_0$  and  $h/D$ . In order to identify the transition between the two regimes in a consistent and quantitative manner, the total number of fingers,  $n$ , (determined by the number of local minima in  $R_b$ ) at  $R \approx 10$  cm has been extracted for varying  $\phi_0$  and  $h/D$ . For given  $h/D$ ,  $n$  sharply increases for increasing  $\phi_0$  and plateaus to a relatively constant value for large  $\phi_0$  (Fig. 4(a)). In corroboration with the videos, this point of transition in  $n$  reliably marks the boundary between ‘no fingering’ versus ‘fingering’ regimes. For instance, at  $h/D = 10.2$ , the interface consists of approximately 20 fingers for  $\phi_0 = 0.23 - 0.24$ , which more than doubles for  $\phi_0 \geq 0.25$ . Accordingly,  $\phi_0 = 0.23 - 0.24$  is considered the transition regime.

Based on the values of  $n$ , we systematically determine fingering regimes and summarize them in a  $\phi_0 - h/D$  phase diagram. In Fig. 4(b), the square and triangle symbols correspond to ‘no fingering’ and ‘fingering’ regimes, respectively, while ‘ $\times$ ’ indicates the transition between the two. For large  $h/D \geq 10$  or the “continuum” limit, the onset of fingering appears to coincide with  $\phi_0 \approx 0.24$ , independent of  $h/D$ . This  $h/D$ -independent behavior is also evident in the number of fingers; for  $h/D \geq 10$ ,  $n$  plateaus at around 50, while it reaches up to 80 for smaller  $h/D$ . Interestingly, in addition to an increase in  $n$ , the fingering initiates at lower  $\phi_0$  as  $h/D$  decreases. This alludes to two possible effects that affect fingering: the effects of wall confinement (*i.e.* small  $h/D$ ) and the increased injection velocity that scales as  $Q/(rh)$ . To decouple the two effects, additional experiments have been conducted in which the injection velocity is kept constant (by adjusting  $Q$  for varying  $h$ ). The results reveal that decreasing  $h$  at a constant injection velocity induces fingering at a lower value of  $\phi_0$ , confirming the effects of wall confinement. On the other hand, the increased velocity is shown to cause fingering to initiate at a larger radius; this transient nature of fingering is beyond the scope of this manuscript and will be addressed as future work.

To experimentally confirm the particle accumulation, we measure the depth-averaged volume fraction  $\bar{\phi}$ , as a function of the radial position,  $r$ , by extracting the light intensity,  $I$ , via MATLAB image processing tools. Note that, in order to eliminate the effects of non-uniformity in lighting on  $I$ , the background image prior to

injection has been systematically subtracted from all images. The relationship between  $I$  and  $\bar{\phi}(r)$  is given in [34] as:

$$k \frac{\log \frac{I(r)}{I_{\min}}}{\log \frac{I_{\max}}{I_{\min}}} = \bar{\phi}(r), \quad (2)$$

where,  $I_{\min}$  and  $I_{\max}$  are the minimum and maximum intensity values of a given image, respectively. The empirical parameter,  $k$ , in Eq. (2) is obtained by integrating  $\bar{\phi}(r)$  from the center to the fluid interface and satisfying mass conservation, such that

$$\int_0^R 2\pi \bar{\phi} r dr = \phi_0 \pi R^2, \quad (3)$$

in which  $R$  is used in lieu of  $R_b(s)$ . In order to discard the injection hole area, the lower limit of the integral in Eq. (3) is set to be a non-zero value, which is negligibly small compared to  $R$ . Fig. 5 demonstrates typical  $\bar{\phi}(r)$  profiles evolving over time for two different values of  $\phi_0$ : (a)  $\phi_0 = 0.11$  that falls in the no fingering regime and (b)  $\phi_0 = 0.32$  with clear fingering. For both cases, the particle volume fraction at the entrance is consistently lower than  $\phi_0$  and rises as  $r \rightarrow R$ . This rise in  $\bar{\phi}$  near the interface is notably steeper for larger  $\phi_0$  and is preceded by the region of constant  $\bar{\phi}$ . Interestingly, Fig. 5(a) suggests that the increase in  $\bar{\phi}$  over  $r$  alone does *not* guarantee the occurrence of fingering.

### 3. Continuum model

#### 3.1. Fingering mechanism

Particle-induced viscous fingering is caused by the accumulation of particles on the meniscus, as described in Fig. 6(b). This increase in particle concentration directly correlates to an increase in the effective suspension viscosity, which results in *miscible* viscous fingering and subsequent formation of particle clusters (labelled as C in Fig. 6(d)). Finally, the interface deforms due to a greater flow resistance through viscous clusters (C) relative to the surrounding medium (D) (see Fig. 6(e)). Therefore, as shown in Fig. 3, the particle clusters and fingering patterns on the interface are perfectly correlated from its initial appearance over time. Furthermore, if more particles collect near the interface with increasing  $\phi_0$ , more pronounced interfacial deformations and particle clustering are observed. Therefore, the key to understand particle-induced fingering lies in the fundamental understanding of the particle accumulation mechanism. However, it is important to note that the particle accumulation on the interface is a bare *minimum* condition for fingering, not necessarily a sufficient one in itself, as demonstrated in Fig. 5(a), and requires further investigation.

Two physical mechanisms behind the particle accretion on the meniscus have been identified, originally in the context of the

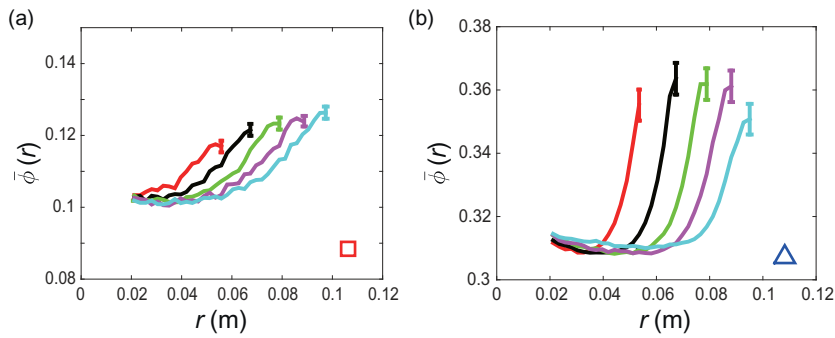


**Fig. 5.** Profile of particle volume fraction at  $h/D = 10.2$  and  $\phi_0 = 0.11$  (a) and  $\phi_0 = 0.32$  (b), respectively. In both plots, the depth-averaged local volume fraction  $\bar{\phi}(r)$  increases in  $r$ . At  $\phi_0 = 0.32$ , the curve increases more sharply, preceded by a notably constant region of  $\bar{\phi}$ , compared to the  $\phi_0 = 0.11$  case that shows a more gradual increase. The error in  $\bar{\phi}_0$  as a result of an estimated 1% error in  $l$  has been computed to be approximately  $\pm 0.002$  for all times and  $r$  and included as error bars.

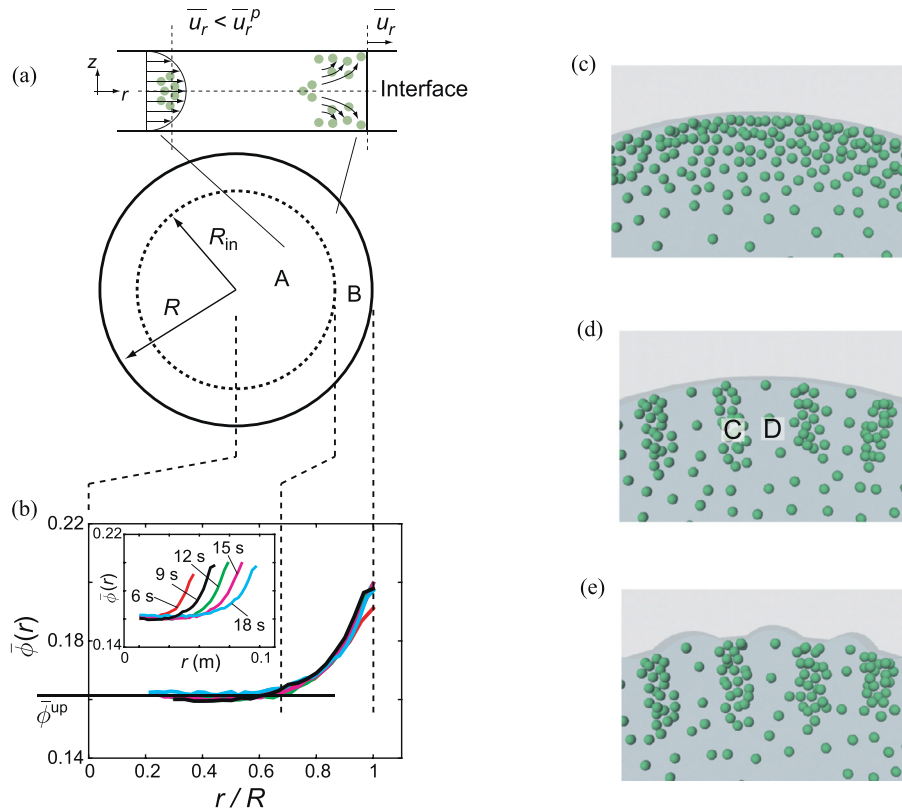


**Fig. 6.** (a) The radial particle-laden flow is divided into an upstream region (A) versus downstream region (B). In region A, the flow can be assumed to be steady and unidirectional, resulting in a simple 1D model based on the suspension balance approach. The particle dynamics in region B involves the effects of a fountain flow and is not straightforward to model at this stage. (b) The plot of  $\bar{\phi}$  versus  $r/R$  for  $\phi_0 = 0.17$  and  $h/D = 10.2$  that clearly exhibits an upstream region A over which  $\bar{\phi}$  is constant followed by B over which  $\bar{\phi}$  steeply rises. (c)–(e) Schematic illustrating the sequence of events that lead to fingering: (c) particles collect near the interface as they move faster than the suspension; (d) the concentration gradient yields an effective viscosity gradient that leads to miscible fingering and particle clustering; (e) the relatively slow flow through clusters causes interfacial deformations.

particle-laden flow in a tube: *particle-entrainment* in the “fountain” flow and *shear-induced migration* in the fully-developed upstream flow [17,18,21]. Karnis and Mason found that the fountain flow near the meniscus diverts particles that approach the interface towards the tube walls; however, finite-sized particles become re-entrained into the fountain flow instead of being swept onto the walls, leading to particle accumulation [17]. Accordingly, this wall exclusion effect is supposed to vanish in the limit of vanishingly small particles, or in the continuum limit.

Surprisingly, Chapman demonstrated experimentally that the meniscus enrichment is present even in the continuum limit due to particle migration far upstream of the interface [18]. Shear-induced migration refers to the particle diffusion from the re-

gions of high shear (i.e. near channel walls where particles are more likely to collide) to those of low shear in a fully-developed, pressure-driven flow [19,20]. Hence, as illustrated in Fig. 6(a), upstream of the interface, there are more particles near the centerline where the flow is the fastest, leading to a net flux of particles towards the interface that is moving at the mean suspension velocity. Therefore, this net flux of particles upstream of the interface leads to the non-zero accumulation of particles near the interface, even in the continuum limit in which the wall exclusion effects are negligible.

The analogous particle accretion phenomenon that drives the interfacial instability is also observed in our current Hele-Shaw geometry, as it has previously been shown in [1,16]. While the actual

mechanism behind particle accretion may be some combination of particle dynamics in the fountain flow and in the fully-developed flow, we presently focus on the effects of shear-induced migration upstream of the interface, which should be dominant in the continuum limit. We hereby define the ratio of the upstream mean particle speed,  $\bar{u}_r^p$ , to that of the suspension,  $\bar{u}_r$ , in the following way:

$$\beta \equiv \frac{\bar{u}_r^p}{\bar{u}_r} = \frac{(\bar{\phi}h)^{-1} \int_{-h/2}^{h/2} u_r^p \phi dz}{h^{-1} \int_{-h/2}^{h/2} u_r dz}, \quad (4)$$

where  $\bar{\phi}(r) = h^{-1} \int_{-h/2}^{h/2} \phi dz$ , and  $u_r$  and  $u_r^p$  denote local suspension and particle radial velocities, respectively. As previously explained, the value of  $\beta$  must be greater than 1 far upstream of the interface, in order for the particle accretion and fingering to occur. In addition,  $\beta$  qualitatively corresponds to the *rate* of particle accumulation on the interface, while the detailed particle concentration near the interface is strongly coupled to the fountain flow [17] (i.e. regime B in Fig. 6(a)), which is beyond the scope of the paper. Therefore, we will theoretically verify this necessary condition for particle accumulation (i.e.  $\beta > 1$ ), by deriving the expression of  $\beta$  as a function of  $\phi_0$  in the upstream regime away from the interface (A in Fig. 6(a)).

### 3.2. Problem formulation

In order to compute  $\beta$  that depends on  $\phi$  and velocity profiles, we model the particle-laden flow as a continuum based on the suspension balance approach [22]. The suspension balance method [22] considers the conservation of mass and momentum of both the overall suspension and the particulate phase in the low Reynolds number limit. Then, the governing equations are given as follows: for the suspension,

$$\nabla \cdot \mathbf{u} = 0, \quad (5)$$

$$\nabla \cdot \boldsymbol{\Sigma} = 0, \quad (6)$$

and for the particulate phase,

$$\frac{\partial \phi}{\partial t} + \nabla \cdot (\phi \mathbf{u}^p) = 0, \quad (7)$$

$$\nabla \cdot \boldsymbol{\Sigma}^p + \mathbf{F} = 0, \quad (8)$$

where  $\boldsymbol{\Sigma}$  and  $\boldsymbol{\Sigma}^p$  correspond to the total stress tensors of the suspension and particulate phase, respectively. The inter-phase drag force,  $\mathbf{F}$ , is given by

$$\mathbf{F} = -\frac{18\eta_1}{D^2} \frac{\phi}{f(\phi)} (\mathbf{u}^p - \mathbf{u}), \quad (9)$$

where the hindrance function,  $f(\phi)$  has an empirical form,  $f(\phi) = (1 - \phi)^n$ , with  $n \approx 5.1$  in the Stokes flow [35]. Note that, specific to our current geometry, the governing equations will be considered in the cylindrical coordinate system, such that the suspension velocity vector is given by  $\mathbf{u} = (u_r, u_\theta, u_z)$ ;  $\mathbf{u}^p$  refers to the velocity vector of the particulate phase.

The suspension and particulate phase are coupled through the constitutive relationships of the stress tensors, namely,

$$\boldsymbol{\Sigma} = -p\mathbf{I} + \eta_1[\nabla \mathbf{u} + \nabla \mathbf{u}^\top] + \boldsymbol{\Sigma}^p, \quad (10)$$

$$\boldsymbol{\Sigma}^p = \boldsymbol{\Sigma}_n^p + (\eta_s(\phi) - \eta_1)[\nabla \mathbf{u} + \nabla \mathbf{u}^\top], \quad (11)$$

where  $p$  is the suspension pressure, and the effective suspension viscosity,  $\eta_s$ , is empirically given as

$$\eta_s(\phi) = \eta_1 \frac{\exp(-2.34\phi)}{(1 - \phi/\phi_m)^3}, \quad (12)$$

valid even for dense suspensions [36], where  $\phi_m = 0.62$  is the maximum packing fraction. Furthermore, the particulate stress,  $\boldsymbol{\Sigma}^p$ , consists of the viscously generated normal stress,  $\boldsymbol{\Sigma}_n^p \propto \eta_n \dot{\gamma}$ , where  $\dot{\gamma}$  is the shear rate and  $\eta_n$  refers to the effective normal viscosity [36,37]:

$$\frac{\eta_n}{\eta_s} = \frac{0.75(\frac{\phi}{\phi_m})^2(1 - \frac{\phi}{\phi_m})^{-2}}{1 + 2.5\phi_m(1 - \frac{\phi}{\phi_m})^{-1} + 0.1\frac{\phi^2}{\phi_m}(1 - \frac{\phi}{\phi_m})^{-2}}. \quad (13)$$

### 3.3. Steady, thin-film model

In the upstream regime (A) away from the interface, it is reasonable to assume a steady state suspension flow, so that the governing equations for the particulate phase yield  $\nabla \cdot \boldsymbol{\Sigma}^p = 0$ , and  $\mathbf{u}^p - \mathbf{u} = 0$ . Furthermore, in the lubrication limit (i.e.  $\partial/\partial r \ll \partial/\partial z$ ) and assuming axisymmetry (i.e.  $\partial/\partial \theta = 0$ ), the particulate governing equation reduces to

$$0 = \frac{d}{dz}(-\eta_n \dot{\gamma}), \quad (14)$$

where  $\dot{\gamma} = du_r/dz$  in the thin-film limit; physically, this equation implies that the particles must arrange themselves in the  $z$ -direction in such a way that the normal stress is constant throughout the thin film. Under the same assumptions, the suspension momentum equation reduces to

$$\frac{dp}{dr} = \frac{d}{dz}(\eta_s \dot{\gamma}). \quad (15)$$

Integrating both sides with respect to  $z$ , subject to the boundary condition,  $\dot{\gamma}(z=0) = 0$ , yields  $(dp/dr)z = \eta_s \dot{\gamma}$ . Hence, by combining Eqs. (14) and (15), we obtain the following ordinary differential equation,

$$\frac{\eta_n}{\eta_s} z = (-\eta_n \dot{\gamma}) \left( \frac{dp}{dr} \right)^{-1} = \text{constant}, \quad (16)$$

which can be solved numerically to yield  $\phi$ ,  $u_r$ , and  $p$ , subject to

$$Q = 2\pi r \int_{-h/2}^{h/2} u_r dz, \quad (17)$$

$$Q\phi_0 = 2\pi r \int_{-h/2}^{h/2} u_r^p \phi dz, \quad (18)$$

where  $u_r^p = u_r$ . The two conditions above, (17) and (18), ensure the steady flow rate of the mixture,  $Q$ , as well as the uniform concentration,  $\phi_0$ , upon injection.

The resultant local volume fraction,  $\phi(z)$ , and the mixture velocity profile,  $u_r$ , are plotted in Fig. 7, which qualitatively match the previous results of a fully-developed 1D suspension flow [22,38,39]. Due to shear-induced migration, or, equivalently, to ensure constant particulate normal stress, the particle concentration is found to be higher near the centerline ( $z=0$ ) than near the wall ( $z=h/2$ ). Unlike the diffusive flux model [39], the particle concentration at  $z=0$  remains below  $\phi_m$  for the range of  $\phi_0$  considered (Fig. 7(a)). The corresponding dimensionless velocity profile,  $u_r/\bar{u}_r$ , is plotted in Fig. 7(b) and exhibits the blunting of the velocity near  $z=0$ , due to a higher particle concentration at the centerline, also consistent with previous findings [22,38,39].

### 3.4. Connection to fingering

Going back to the necessary condition for particle accumulation and fingering, we expect the ratio of the mean particle velocity to the mean suspension velocity,  $\beta$ , to be greater than 1. As a direct result of higher  $\phi$  near  $z=0$  where the flow is the fastest,

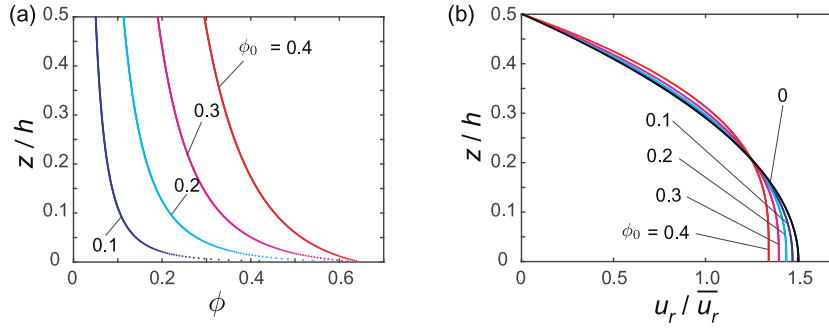


Fig. 7. Profiles of (a) local  $\phi$  and (b) normalized radial velocity,  $u_r/\bar{u}_r$ , along the  $z$ -axis for varying  $\phi_0$ .

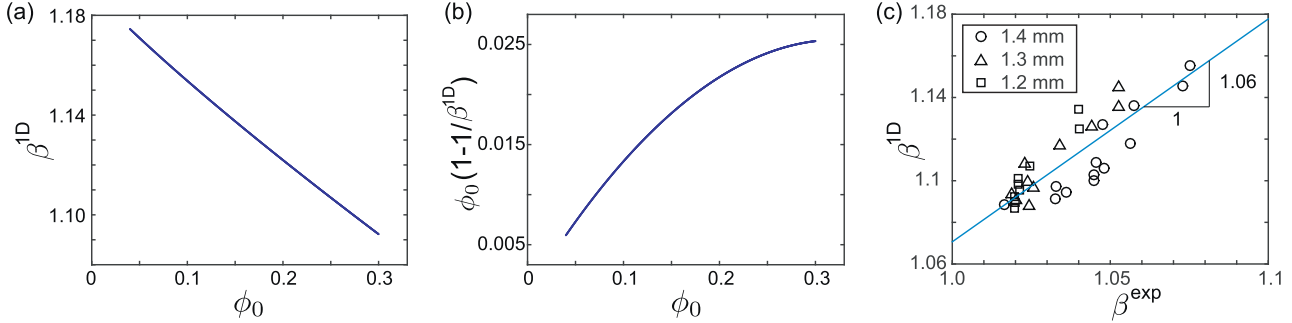


Fig. 8. Plots of (a)  $\beta^{1D}$  and (b)  $\phi_0(1 - 1/\beta^{1D})$  with varying  $\phi_0$ , where  $\beta^{1D}$  denotes  $\beta$  derived based on the suspension balance model. (c) The values of  $\beta^{1D}$  reasonably match those obtained experimentally (i.e.  $\beta^{\text{exp}}$ ) for varying  $\phi_0$  and  $h/D$ .

we show in Fig. 8(a) that  $\beta > 1$  for all  $\phi_0$ ; however,  $\beta$  surprisingly decreases with  $\phi_0$ . The latter indicates that the resultant fingering does not generally increase with the rate of particle accumulation on the interface, given by  $\beta$ . Instead, the fingering mechanism is shown to depend on the total amount of particles accumulated on the interface,  $\phi_0(1 - \beta^{-1})$ : the product of the relative particle accumulation rate,  $(\beta - 1)$ , and the depth-average particle concentration in the upstream regime,  $\bar{\phi}^{\text{up}} = \phi_0\beta^{-1}$ , by mass conservation in Eq. (18). As  $\phi_0(1 - \beta^{-1})$  increases, the higher particle concentration and effective viscosity become higher near the interface. As a result, larger  $\phi_0(1 - \beta^{-1})$  is more likely to cause miscible fingering and interfacial deformations. As shown in Fig. 8(b),  $\phi_0(1 - \beta^{-1})$  increases with  $\phi_0$ ; thus, fingering becomes more pronounced as  $\phi_0$  increases, as shown in Fig. 2. Note that there is no explicit dependence on  $h/D$  in the continuum model, which qualitatively explains why the fingering onset appears to be independent of  $h/D$  for  $h/D \geq 10$ , as shown in Fig. 4(b).

As  $\bar{\phi}^{\text{up}}$  can be directly measured from experimental results shown in Fig. 5, we can thus obtain the value of  $\beta$  experimentally (denoted with superscript ‘exp’) and compare it to that derived theoretically (denoted with superscript ‘1D’). The resultant plot of  $\beta^{1D}$  versus  $\beta^{\text{exp}}$  shows a reasonable collapse onto a single line of the slope = 1.06, for all values of  $\phi_0$  and  $h/D$  considered. Finally, the average concentration of downstream region,  $\phi_{\text{av}}$ , is derived as  $\phi_{\text{av}} = \phi_0 + \phi_0(1 - \beta^{-1})R_{\text{in}}^2/(R^2 - R_{\text{in}}^2)$  by volume conservation of particles. According to Fig 6(b), the size of the upstream regime,  $R_{\text{in}}$ , collapses onto a single line for all times when scaled by  $R$ . This implies that  $R_{\text{in}} \propto R$ , which leads to  $\phi_{\text{av}} - \phi_0 \propto \phi_0(1 - \beta^{-1})$ . Therefore, for given  $\phi_0$ , the average downstream concentration,  $\phi_{\text{av}}$ , does not change over time, while the local particle concentration near the interface cannot be computed without resolving the fountain flow.

#### 4. Discussion

In summary, we hereby present the particle-induced viscous fingering when a suspension of neutrally buoyant particles and oil

is injected radially into a Hele-Shaw cell, which was previously observed in [1,16]. This surprising fingering phenomenon is directly due to the presence of particles, as the injection of a clear oil into a Hele-Shaw cell is inherently stable. Building on the previous work [1,16], we experimentally quantify the critical volume fraction,  $\phi_0$ , at which fingering initiates for given  $h/D$ , by measuring the total number of fingers at a fixed suspension radius. In addition, we experimentally measure the depth-average particle concentration,  $\bar{\phi}$ , which clearly shows that the particles accumulate near the interface. This increase in particle concentration near the interface corresponds to a higher effective viscosity; this viscosity gradient results in miscible fingering and subsequent interfacial deformations.

In tandem to experiments, we use the suspension balance approach to model the particle-laden flow as a continuum valid in the limit of  $D/h \ll 1$ , far upstream of the interface where we can reasonably assume a fully-developed, unidirectional flow. This simple model is motivated by the fact the particle accumulation on the interface arises from shear-induced migration of particles upstream of the interface. Specifically, we compute  $\beta$  which is the measure of the particle accumulation rate on the interface as a function of  $\phi_0$ . Our results indicate that, while  $\beta$  must be greater than 1 for fingering to occur, fingering depends more directly on the total amount of particles collected near the interface, given by  $\phi_0(1 - \beta^{-1})$ , instead of  $\beta$  alone.

Although the particle-induced viscous fingering shares similar fundamental physics with miscible viscous fingering for clear fluids, some key differences exist. Notably, while miscible fingering occurs inside the suspension flow, “de-fingering” must also take place on the interface, since the air viscosity outside the interface is much lower than the suspension viscosity. This stabilizing effect suppresses the finger growth; thus, the particle-induced viscous fingering exhibits relatively dull and short fingers, distinct from narrow and long fingering patterns observed in the clear fluid counterpart [40]. During “de-fingering”, two adjacent fingers merge, leaving a particle cluster between the fingers. This process is repeatedly observed, splitting each finger into mostly two fin-

gers, which is part of our on-going investigation. Additional on-going work includes performing a stability analysis of the particle-laden flow to identify the critical value of  $\phi_0$  that leads to miscible fingering. While our current simple model successfully validates the effect of shear-induced migration on particle accumulation, further analysis is needed to predict the onset of fingering as well as to understand the particle dynamics in the fountain flow region. Finally, complete understanding of the effect of the wall confinement on fingering may necessitate full numerical simulations based on Stokesian dynamics [41].

Overall, the interfacial instability in the suspension flow is relevant for various geophysical flows as well as numerous applications both in the energy sector (i.e. enhanced oil recovery) and biomedical field. Despite its significance, the coupled dynamics between the fluid-fluid interface and particles remains relatively unexplored, and this work represents initial steps towards elucidating this coupling. The results of this study can be expanded to other types of flows involving suspension film flows, such as suspension drop dynamics on a surface [42,43], suspension spreading in a rheometer [16], or blood flows in a thin film geometry [44].

### Acknowledgments

The authors wish to thank the Texas A&M Engineering Experiment Station (TEES) and NSF-REU program (NSF-EEC 1263196) for financial support. The authors would like to especially acknowledge undergraduate students, Celina Lopez, Grace Fomani, and Dillon Strack, for their help in data acquisition, as well as a PhD student, Yun Chen, for fruitful discussions and comments.

### References

- [1] H. Tang, W. Grivas, D. Homentcovschi, J. Geer, T. Singler, Stability considerations associated with the meniscoid particle band at advancing interfaces in hele-shaw suspension flow, *Phys. Rev. Lett.* 85 (2000) 2112–2115.
- [2] P. van Meurs, The use of transport three-dimensional models for studying the mechanism of flow process in oil reservoirs, *Trans. AIME* 210 (1957) 295–301.
- [3] P.G. Saffman, G. Taylor, The penetration of a fluid into porous medium or hele-shaw cell containing a more viscous liquid, *Proc. R. Soc. London, Ser. A* 245 (1958) 312–329.
- [4] R.L. Chouke, P. van Meurs, C. van der Poel, The instability of slow, immiscible, viscous liquid-liquid displacements in permeable media, *Pet. Trans. AIME* 216 (1959) 188–194.
- [5] D. Pihler-Puzovic, R. Perillat, M. Russell, A. Juel, M. Heil, Modelling the suppression of viscous fingering in elastic-walled hele-shaw cells, *J. Fluid Mech.* 731 (2013) 162–183.
- [6] M.G. Moore, A. Juel, J.M. Burgess, W.D. McCormick, H.L. Swinney, Fluctuations in viscous fingering, *Phys. Rev. E* 65 (2002) 030601.
- [7] G.M. Homsy, Viscous fingering in porous media, *Ann. Rev. Fluid Mech.* 19 (1987) 271–311.
- [8] D.A. Reinelt, The primary and inverse instabilities of directional viscous fingering, *J. Fluid Mech.* 285 (1995) 303–327.
- [9] E. Ben-Jacob, H. Shmueli, O. Shochet, A. Tenenbaum, Adaptive self-organization during growth of bacterial colonies, *Physica A: Stat. Mech. Appl.* 187 (1992) 378–424.
- [10] A.K. McAllister, Cellular and molecular mechanisms of dendrite growth, *Cereb. Cortex* 10 (2000) 963–973.
- [11] C. Clanet, G. Searby, First experimental study of the darrieus-landau instability, *Phys. Rev. Lett.* 80 (17) (1997) 3867–3870.
- [12] T.T. Al-Housseiny, H.A. Stone, Controlling viscous fingering in tapered hele-shaw cell, *Phys. Fluids* 25 (2013) 092102.
- [13] A. Lindner, D. Bonn, E.C. Poire, M.B. Amar, J. Meunier, Viscous fingering in non-newtonian fluids, *J. Fluid Mech.* 469 (2002) 237–256.
- [14] P. Tordjeman, Saffman-taylor instability of shear thinning fluids, *Phys. Fluids* 19 (2007) 118102.
- [15] D.H. Vlad, J.V. Maher, Tip-splitting instabilities in the channel saffman-taylor flow of constant viscosity elastic fluids, *Phys. Rev. E* 61 (2000) 5439–5444.
- [16] A. Ramachandran, D.T. Leighton, Particle migration in concentrated suspensions undergoing squeeze flow, *J. Rheol.* 54 (2010) 563–589.
- [17] A. Karnis, S.G. Mason, The flow of suspensions through tubes iv. meniscus effects, *J. Colloid Interf. Sci.* 23 (1967) 120–133.
- [18] B.K. Chapman, Shear-induced migration phenomena in concentrated suspensions, University of Notre Dame, 1990 Ph.D. thesis.
- [19] D. Leighton, A. Acrivos, The shear-induced migration of particles in concentrated suspensions, *J. Fluid Mech.* 181 (1987) 415–439.
- [20] R.J. Phillips, R.C. Armstrong, R.A. Brown, A.L. Graham, J.R. Abbott, A constitutive equation for concentrated suspensions that accounts for shear-induced particle migration, *Phys. Fluids A* 4 (1) (1992) 30–40.
- [21] A. Ramachandran, D.T. Leighton, The effect of gravity on the meniscus accumulation phenomenon in a tube, *J. Rheol.* 51 (2007) 1073.
- [22] P.R. Nott, J.F. Brady, Pressure-driven flow of suspensions - simulation and theory, *J. Fluid Mech.* 275 (1994) 157–199.
- [23] Particle-laden viscous thin-film flows on an incline: experiments compared with a theory based on shear-induced migration and particle settling.
- [24] N. Murisic, B. Pausader, D. Peschka, A.L. Bertozzi, Dynamics of particle settling and resuspension in viscous liquid films, *J. Fluid Mech.* 717 (2013) 203–231.
- [25] F. Boyer, E. Guazzelli, O. Pouliquen, Unifying suspension and granular rheology, *Phys. Rev. Lett.* 107 (2011) 188301.
- [26] B. Lecampion, D.I. Garagash, Confined flow of suspensions modelled by a frictional rheology, *J. Fluid Mech.* 759 (2014) 197–235.
- [27] S. Dagois-Bohy, S. Hormozi, E. Guazzelli, O. Pouliquen, Rheology of dense suspensions of non-colloidal spheres in yield-stress fluids, *J. Fluid Mech.* 776 (2015) R2.
- [28] C. Ness, J. Sun, Shear thickening regimes of dense non-brownian suspensions, *Soft Matter* 12 (2016) 914–924.
- [29] K. Zhang, A. Acrivos, Viscous resuspension in fully developed laminar pipe flows, *Intl J. Multiphase Flow* 20 (1994) 579–591.
- [30] S. Lee, Y. Stokes, A. Bertozzi, Behavior of a particle-laden flow in a spiral channel, *Phys. Fluids* 26 (2014) 043302.
- [31] J.F. Morris, J.F. Brady, Pressure-driven flow of a suspension: buoyancy effects, *Intl J. Multiphase Flow* 24 (1998) 105–130.
- [32] F. Boyer, O. Pouliquen, E. Guazzelli, Dense suspensions in rotating-rod flows: normal stresses and particle migration, *J. Fluid Mech.* 686 (2011) 5–25.
- [33] T.G. Beckwith, R.D. Marangoni, *Mechanical Measurements*, fifth ed., Addison-Wesley, New York, 1993.
- [34] G. Grasa, J.C. Abanades, A calibration procedure to obtain solid concentrations from digital images of bulk powders, *Powder Tech.* 114 (2001) 125–128.
- [35] R.H. Davis, A. Acrivos, Sedimentation of noncolloidal particles at low reynolds numbers, *Annu. Rev. Fluid Mech.* 17 (1985) 91–118.
- [36] I.E. Zarraga, D.A. Hill, D.T. Leighton, The characterization of the total stress of concentrated suspensions of non-colloidal spheres in newtonian fluids, *J. Rheol.* 44 (2000) 185–220.
- [37] J.F. Morris, F. Boulay, Curvilinear flows of noncolloidal suspensions: The role of normal stress, *J. Rheol.* 43 (1999) 1213.
- [38] R.M. Miller, J.F. Morris, Normal stress-driven migration and axial development in pressure-driven flow of concentrated suspensions, *J. Nonnewton. Fluid Mech.* 135 (2006) 149–165.
- [39] J.F. Brady, Macroscopic modeling of viscous suspension flows, *Appl. Mech. Rev.* 6 (1994) S229–S235.
- [40] L. Paterson, Radial fingering in a hele shaw cell, *J. Fluid Mech.* 113 (1981) 513–529.
- [41] J.W. Swan, J.F. Brady, The hydrodynamics of confined dispersions, *J. Fluid Mech.* 687 (2011) 254–299.
- [42] M. Nicolas, Spreading of a drop of neutrally buoyant suspension, *J. Fluid Mech.* 545 (2005) 271–280.
- [43] V. Grishaev, C.S. Iorio, F. Dubois, A. Amirfazli, Complex drop impact morphology, *Lanmuir* 31 (2015) 9833–9844.
- [44] D. Brutin, B. Sobac, C. Nicloux, Influence of substrate nature on the evaporation of a sessile drop of blood, *J. Heat Transfer* 134 (2012) 061101.